Stochastic geometry of polygonal networks: An alternative approach to the hexagon-square transition in Bénard convection

Uwe Thiele
Institute for Material Science, Dresden University of Technology, 01062 Dresden, Germany

Kerstin Eckert
Center for Physical Fluid Dynamics, Dresden University of Technology, 01062 Dresden, Germany

(Received 5 May 1997; revised manuscript received 3 June 1998)

We apply stochastic geometry to the transition from hexagonal to square cells recently observed in surface-tension-driven Bénard convection. In particular we study the metric and topological evolution of Bénard patterns as a function of the temperature difference, ΔT, across the layer. The preference of square Bénard cells at higher ΔT is a consequence of both a higher efficiency in heat transfer and more favorable metric properties. Most notably, the perimeter-area ratio of a square cell exceeds that of a hexagonal cell by an unexpectedly high value. From a topological point of view, the Bénard pattern obeys the Aboav-Weaire law at all times, even in the presence of threefold and fourfold vertices. The regimes above and below the transition are characterized by different topological correlations between neighboring cells. With the appearance of fourfold vertices, the topological correlation changes from negative to positive. [S1063-651X(98)14709-8]

PACS number(s): 47.20.Dr, 47.54.+r, 02.50.−r, 64.60.Cn

I. INTRODUCTION

Three-dimensional cellular structures based on two-dimensional polygonal patterns are widespread in nature. In biology, they appear, e.g., in corn cobs and epidermal tissue. Many metallic materials are polycrystalline. Etching their surfaces reveals the polygonal arrangement of the small single crystals. In hydrodynamics polygonal structures arise, e.g., from surface-tension-driven Bénard convection and Rayleigh-Bénard convection in non-Boussinesq fluids.

To analyze such patterns we employ the stochastic geometry of polygonal networks (SGPN). Historically, the first polygonal structures investigated by SGPN were biological tissues [1–6]. Later research focused on clusters of metal grains, soap froth, and the similarity between their structures and evolution [7–14]. For a detailed review of stochastic networks in different physical systems we refer to [15].

While the application of SGPN to soap froth and polycrystals has been fruitful, we are aware of only one application to polygonal convective patterns [16]. However, these methods are particularly suited to geometrical studies of the evolution of surface-tension-driven Bénard (STDBC) or Bénard-Marangoni convection.

In the last decade STDBC has received considerable attention. Since the first experiments of Bénard [17] STDBC has been associated with hexagonal patterns. While important features of the moderately nonlinear regime, like the onset of convection [18,19], wave number selection [20,21], and evolution of disorder [22] are well understood, the behavior in the strongly nonlinear regime of STDBC has only recently received a comprehensive analysis. References [23–25] showed that beyond a certain distance above the threshold of the primary instability, square convection cells rather than the seemingly ubiquitous hexagons are persistent and dominant.

We reexamine the transition from hexagonal to square Bénard cells by means of SGPN, because none of the previous studies elucidated the control parameter dependence of the metric and topological properties of the Bénard cells. Instead most quantified the wave number or the disorder. Since the hexagon-square-transition resembles an order-disorder transition, we next review three existing approaches to quantify disorder.

The first approach [26,27,22] that introduces different measures of disorder such as the radial and orientational correlation functions and special disorder functions, accounts for displacements and distortions of cells caused by defects in a hexagonal pattern. Since disorder is always measured with respect to an ideal hexagonal pattern, an adequate description of the transition between convective states of different symmetry occurring at higher super-criticality is not possible.

The second method calculates the minimal spanning tree of the pattern, which is the shortest possible graph that connects all centers of mass of the convection cells. The branch length histogram is unique for the arrangement of cell centers. The evolution of convection networks is characterized in terms of the normalized average branch length and the standard deviation of the branch length distribution [28]. The information contained in both quantities is very restricted and does not elucidate the topological structure of the network. Large cells are underrepresented because the minimal spanning tree prefers to use small cells for its main branches.

The third approach describes convection cells by means of the crystallography in cylindrical symmetry [29,30]. The main assumptions are weak disorder and the occurrence of threefold vertices only. This approach cannot handle patterns characterized by vertices with coordination number four as for square Bénard cells.

To summarize, the three approaches apply to the weakly nonlinear evolution of the hexagonal pattern, but not to the transition between patterns of different symmetry. This gap can be bridged by SGPN. Furthermore, SGPN allows the comparison between polygonal patterns in hydrodynamics

TABLE I. Metric and topological quantities used for the characterization of cellular networks.

Quantity	Symbol	Type
Cell area	a	metric
Cell perimeter	π	metric
Side length	l	metric
Angle between two sides	ω	metric
Vertex coordination number	ν	topological
Side number	n	topological

and other networks such as, e.g., soap froths, epidermal tissue, or honeycombs. These patterns have a vertex coordination number of three. As long as STDBC occurs in hexagonal cells with single defects the Bénard pattern fulfills the general topological relations derived for networks with threefold vertices [16]. We ask here whether these relations apply also to STDBC patterns with appearance of square cells, i.e., fourfold vertices.

The mathematics of stochastic two-dimensional networks is introduced in Sec. II A. Next we discuss STDBC including the recently observed hexagon-square transition. In Sec. III we apply SGPN to the metric and topological changes of Bénard cells during this transition. We calculate the topological correlations between neighboring Bénard cells and discuss their differences from those of other naturally occurring networks (Sec. III C). We find both positive and negative correlations between the topologies of neighboring cells. Finite size effects are estimated in Sec. III D.

II. METHODS

A. Mathematical tools for two-dimensional patterns

A cellular pattern is a dense, space-filling arrangement of n-sided polygons. The number of sides, n, of the individual polygons varies. To analyze such cellular patterns we use stochastic geometry [31–33], based on the statistical distributions of the network-variables both metric and topological (Table I). Imagine a cellular pattern artificially deformed by applying a force at one side. The metrics of the pattern change while the values of the topological quantities remain the same. General relations exist between the mean values of the corresponding distributions of the network-variables and the intensive quantities of the network. The intensive quantities (Table II) are v, k, and s, the densities of vertices, cell sides, and cells, respectively. The most important parameters of the distributions f are the mean value,

$$\langle f\rangle=\frac{1}{N}\sum_{i=1}^{N} f_i,$$

TABLE II. Intensive network quantities. N_v, N_k, and N_c are the numbers of vertices, cell sides, and cells, respectively, and A is the area filled by the network.

Density	Symbol	Formula
Density of vertices	v	N_v/A
Density of sides	k	N_k/A
Density of cells	s	N_c/A

and the second moment,

$$\mu_2^f=\frac{1}{N}\sum_{i=1}^{N} (f_i-\langle f\rangle)^2.$$

f_i is the value of f for cell number i. We call the mean values and the intensive quantities the first order characteristics of the network. Normalized second moments are divided by the square of the mean value $\langle f\rangle^2$.

The distributions of the quantities in Table I and the densities in Table II depend on each other but only a few dependencies are known. Exact relations for the mean values and the densities exist in the limit of infinite networks only. The most important are (for details and proofs see [33] and references therein):

$$\langle a\rangle=\frac{\langle n\rangle}{2k}=\frac{1}{s}, \tag{1}$$

$$v=\frac{2k}{\langle \nu\rangle}, \tag{2}$$

which relate the average number of sides, $\langle n\rangle$, and the density of sides, k, to the average cell area, $\langle a\rangle$ (i.e., to the density of cells, s) [Eq. (1)], and the density of vertices, v, to the density of sides, k, and the average vertex coordination number, $\langle \nu\rangle$ [Eq. (2)]. Together with Euler's relation,

$$v-k+s=0, \tag{3}$$

they lead to

$$\frac{1}{\langle \nu\rangle}+\frac{1}{\langle n\rangle}=\frac{1}{2}. \tag{4}$$

Equation (4) states that $\langle n\rangle$ is exactly six for networks with exclusively threefold vertices and less than six for networks that include vertices with a coordination of four or more. Between the average cell perimeter $\langle \pi\rangle$ and the average side length $\langle l\rangle$ we have the relation

$$\langle \pi\rangle=\langle l\rangle\langle n\rangle. \tag{5}$$

Equations (1)–(5) reduce all first order information on the set of densities and mean values to a triplet, containing one of the densities, one mean value of a topological variable ($\langle n\rangle$ or $\langle \nu\rangle$), and a metric variable characterizing the boundary of the cells ($\langle l\rangle$ or $\langle \pi\rangle$).

A complete characterization of the structure also requires higher moments of the distributions, whose relations are not known. We use the second moment of the distribution of the number of sides μ_2^n, abbreviated μ_2, as a measure of disorder of the network [15].

Correlations among metric and topological quantities can also be considered, e.g., the Aboav-Weaire law for the purely topological correlation between the number of sides of neighboring cells. The relation was introduced for infinite networks with vertex coordination three ($\langle n\rangle=6$) and extended to $\langle n\rangle\neq 6$ to account for finite size effects [34–37]. This law linearly relates $m(n)n$ and n:

$$m(n)n=(\langle n\rangle-a_W)\ n+\langle n\rangle a_W+\mu_2. \tag{6}$$

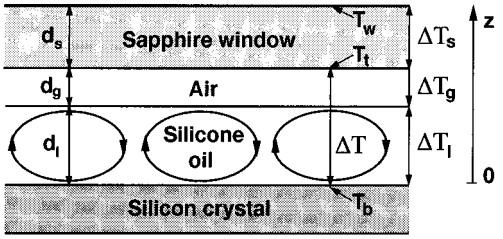

FIG. 1. Schematic of the liquid-air Bénard system: A temperature difference, $\Delta T=\Delta T_l+\Delta T_g$, is maintained across the two layers by isothermal plates. The flow is mainly driven by the temperature dependence of surface tension. The thicknesses of the liquid and air layer are d_l and d_g, respectively.

$m(n)$ stands for the average number of sides of all neighboring cells to a cell with n sides averaged over all n-sided cells. a_W is an empirically determined parameter that quantifies the deviation of the slope from the average number of sides.

Equation (6) holds for disordered patterns like biological cells and soap froth. In these cases a_W is about 1.2, calculated from the data with a weighted least-squares fit. The weights are chosen to be the probabilities p_n to find cells with n sides. a_W is then given by [34,35]

$$a_W=[\langle n\rangle\langle nm(n)\rangle+\mu_2-\langle n^2m(n)\rangle]/\mu_2. \tag{7}$$

Equation (6) also naturally extends the Aboav-Weaire law to networks with nonthreefold vertices.

Phenomenologically the Aboav-Weaire law says that, in the usual case $\langle n\rangle-a_W\approx 5$, on the average one finds cells with few sides beside cells with many sides and vice versa.

The dependencies of the average cell area and perimeter on the number of sides n are linear for the area for biological cells (Lewis' law) and for the perimeter for polycrystals (Feltham's law). Linearity is not clear for soap froth [15,14,37]. Neither relation holds for Bénard cells (Sec. III B 2).

B. The experiment

1. A brief introduction

The experiment consists of a liquid layer heated from below by a horizontal plate of uniform temperature (cf. Fig. 1). The free surface of the liquid is in contact with air, cooled by the upper isothermal plate. The quiescent basic state of the liquid-air layers loses its stability to hexagonal cell convection once the temperature difference, ΔT, between the lower plate and interface exceeds a critical value, ΔT_c. In liquid layers with thickness of the order of 1 mm or less, surface tension dominates buoyancy. Thus, the essential ingredient for STDBC is the variation of surface tension σ with temperature T, approximately,

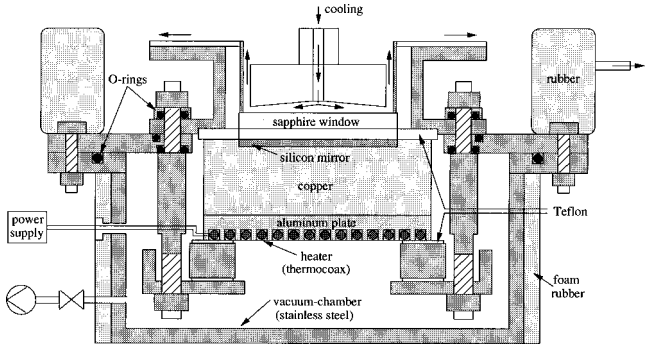

FIG. 2. Schematic section through the experimental apparatus.

$$\sigma=\sigma_0-\gamma(T-T_0), \tag{8}$$

where the temperature coefficient of the surface tension $\gamma=-d\sigma/dT$ is positive for the liquids we used. If a temperature fluctuation generates a hot spot at the free surface, the surface tension decreases according to Eq. (8). As a result, liquid is pulled radially outward to regions of higher surface tension, causing further up-flow in the vicinity of the spot. For sufficient ΔT the rising hot liquid reinforces the temperature disturbance, causing the primary instability.

2. Setup and parameters

Figure 2 shows the apparatus. The container bottom is a polished silicon crystal wafer, 12.5 cm in diameter, on a 5 cm thick copper block with a diameter of 17.5 cm. An aluminum disk of the same diameter containing 4.0 m of a thermo-coax cable (Philips) is pressed from below against the copper block. To minimize lateral heat losses the copper block is placed in a vacuum, and, the outer parts of the chamber are thermally insulated. The liquid layer is confined by an inner plexiglass ring of radius $r=45.2$ mm. A meniscus at the inner ring is avoided by filling it to its total height. The space between this ring and a second ring of larger diameter is filled with the same liquid to minimize lateral temperature gradients. We use a 10 cS silicone oil (NM 10, Hüls AG) with a Prandtl number Pr=100 at $T=25\,^{\circ}$C. Its properties are summarized in Table III.

The liquid thickness d_l is 1.41 mm for an aspect ratio $\Gamma=2r/d_l=64$. The liquid layer is closed from above by a transparent sapphire disk, 12.0 cm in diameter with a thickness $d_s=2.99$ mm, placed on a third, outer ring. The air layer, formed by the difference in height between inner and outer ring, has a thickness $d_g=0.26$ mm.

A special cooling device [38] supplies water with a flow rate of 95 l/h at $18.0\pm 0.01\,^{\circ}$C to the center of the sapphire disk where it flows radially outwards, ensuring axisymmetric cooling. The temperatures of the silicon crystal T_b, and of the sapphire window, T_w, are measured with encapsulated

TABLE III. Properties of the silicone oil NM 10 (Hüls AG) at 25 °C. ν, ρ, κ, λ, α, and γ denote viscosity, density, thermal diffusivity, heat conductivity, thermal expansion coefficient, and temperature coefficient of surface tension.

ν (10^{-4} m^2/s)	ρ (kg/m^3)	κ (10^{-4} m^2/s)	λ_l (W/m K)	α (K^{-1})	γ (N/mK)
0.10	940.0	0.00103	0.134	0.0011	5.9 10^{-5}

quartz crystals. They have a diameter of 1.8 mm and show a highly linear dependence of the resonance frequency on temperature. T_b is controlled with a feedback loop (± 0.005 K) and increased automatically in a quasistatic manner at a rate of 0.08 K/h. Before visualization, T_b is held constant for one horizontal relaxation time, $\tau_h = r^2/\kappa$, approximately 5 h. κ denotes the thermal diffusivity.

The dimensionless control parameter ε, measuring the distance above the threshold of primary instability, is defined as

$$\varepsilon = \frac{\Delta T_{cd} - \Delta T_c}{\Delta T_c}, \tag{9}$$

where ΔT_{cd} is the temperature difference in the conductive regime given by

$$\Delta T_{cd} = \frac{T_b - T_w}{1 + (\lambda_l/d_l)(d_g/\lambda_g + d_s/\lambda_s)}. \tag{10}$$

λ_l, λ_g, and λ_s are the heat conductivities of liquid, air, and sapphire, respectively. For more details we refer to [25].

3. Image processing

We used standard shadowgraph techniques to visualize the convective pattern [39], thresholded into binary pictures, using a QUANTIMET 570 image processing and analysis program (Leica). Thresholding retains the light appearing cell knots (vertices) and edges (sides), which correspond to the down-flow of cold liquid.

The binary pictures are corrected manually before the coordinates of the vertices of every cell and pointers to all neighboring cells are extracted. From this information we calculate the metric and topological quantities only for bulk cells (180 to 250) to avoid perturbing effects introduced by peripheral cells. The quantities include side length, number of sides, cell area, cell perimeter, and angles between the sides (in the following ''side angle'') for all cells. To compute the cell area an n-sided polygon is approximated by $n-2$ triangles.

The digitizing routines split fourfold vertices into two closely spaced threefold vertices and a short side between them. To eliminate spurious sides, vertices separated by less than a defined cutoff length are merged iteratively and interactively to preserve the topology of the network. We determine the cutoff length from the side length distribution for each image. The uncorrected distributions have an unphysical minimum at side lengths comparable to the typical diameter of the vertices that can be identified within an error of 1 pixel. To estimate the error caused by edge elimination, some patterns were corrected with the derived cutoff $\pm$ 1 pixel. The resulting small error together with the finite resolution of the digital images gives the error bars in the plots.

III. RESULTS

Before analyzing metrics and topology of the STDBC pattern in detail we first wish to demonstrate qualitatively the changes in the cellular composition (Fig. 3). Increasing the control parameter ε in a quasistatic manner, a pattern of well-ordered hexagonal cells appears at $\varepsilon = 0$ [18,19,25].

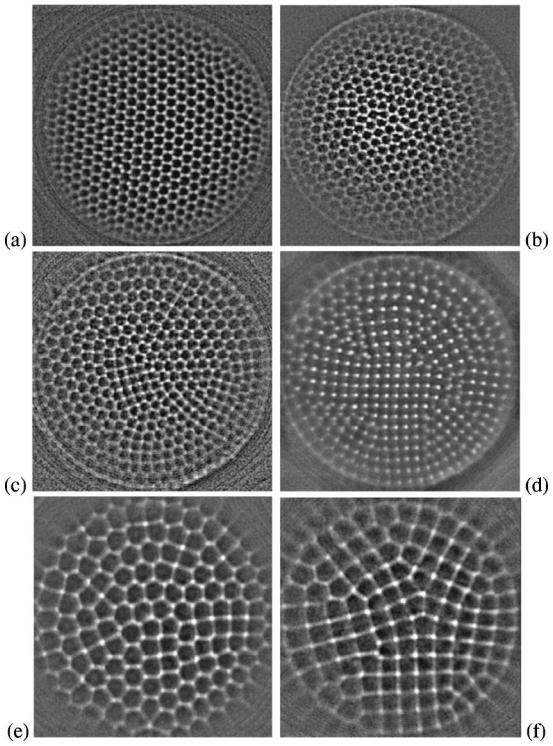

FIG. 3. Changes of the cellular pattern of STDBC with increasing control parameter ε (shadowgraph images) for large aspect ratio ($\Gamma = 64$): (a) hexagonal cells ($\varepsilon = 2.2$), (b) defects in the hexagonal pattern ($\varepsilon = 2.4$), (c) intermediate stage ($\varepsilon = 4.0$), (d) square cells ($\varepsilon = 6.1$), and for medium aspect ratio ($\Gamma = 42$): (e) intermediate stage ($\varepsilon = 4.0$), (f) square cells ($\varepsilon = 5.3$). The parameter are Pr $= 100$, $d_l = 1.41$ mm, $d_g = 0.26$ mm for (a)–(d) and Pr$= 100$, $d_l = 1.56$ mm, $d_g = 0.46$ mm for (e)–(f).

This pattern can be preserved to higher ε under low noise conditions. Figure 3(a) shows an example for $\varepsilon = 2.2$. More typical, however, is the presence of certain types of defects for this ε range [Fig. 3(b)]. These defects mainly cluster into penta-hepta pairs and different kinds of flower defects [40]. Generally, the penta-hepta defect (see Sec. III A) has the highest topological stability. Beyond $\varepsilon_p = 1.5 \pm 0.5$, depending on the layer thickness d_l, the number of pentagonal cells rises as a consequence of a systematic modification occurring in the defect structure [41]. As a result, pentalines of growing order, i.e., increasing numbers of pentagonal cells, are formed [Figs. 3(c) and 3(e)]. Above $\varepsilon_s = 4.2 \pm 0.3$ square convection cells appear. With increasing ε the squares continuously replace the hexagons. An advanced stage of this process is shown in Fig. 3(d). While at the highest ε achieved in the experiments, a small number of hexagons persist between the square cell domains for large aspect ratios, a nearly pure square pattern is obtained for smaller aspect ratios [Fig. 3(e)]. The basic properties of the square Bénard cells have been studied in [25]: The square cells more efficiently transport heat, whereby their wave number exceeds that of hexagonal cells. While the selection of hexagons at the onset of convection can be intuitively understood on the basis of symmetry arguments, the selection of squares is not so obvious. In Sec. III B 3 we demonstrate that their metric properties, as well as their higher transport efficiency, are another reason for the greater efficiency of square cells in strongly nonlinear STDBC.

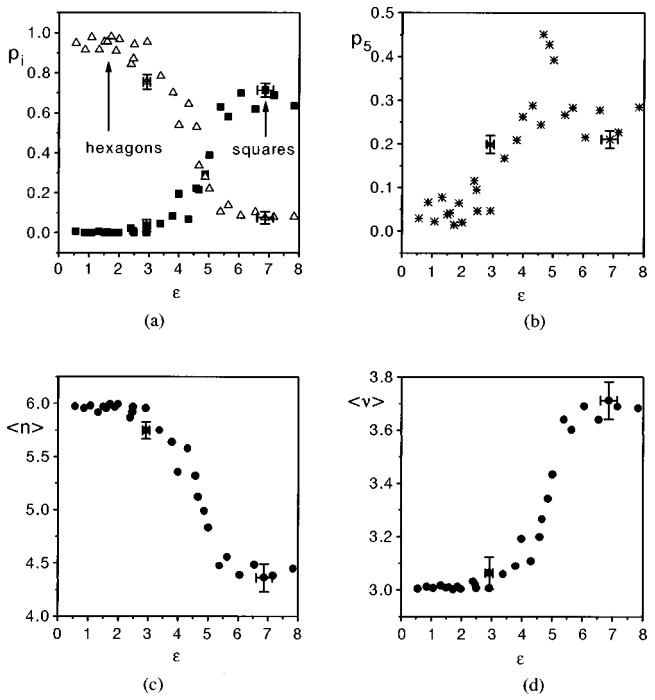

FIG. 4. Evolution of topological quantities with control parameter ε. (a) Probability of hexagonal and square cells, (b) probability of pentagonal cells, (c) average number of sides, (d) average coordination number of vertices.

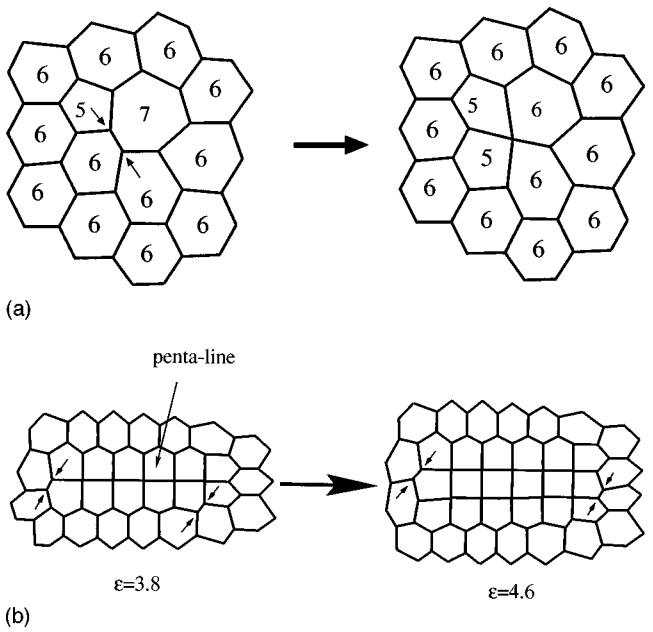

FIG. 5. (a) Transformation of a penta-hepta defect (left) into the 5-5-6-6 cluster (right) having a fourfold vertex at the center. (b) Transformation of a pentaline (left) into a patch of square cells with pentagonal edges (right). Schematic after shadowgraph images. The arrows in (a) and (b) indicate vanishing sides.

A. Topological properties of Bénard cells

The side number distribution gives direct access to the fraction, p_n, of polygonal cells with n sides. The p_n of the main cell types (hexagons, pentagons, and squares) are plotted in Figs. 4(a) and 4(b). The mean values of the distributions, namely, the average number of sides, $\langle n \rangle$, and the average vertex coordination number, $\langle \nu \rangle$, are shown in Figs. 4(c) and 4(d).

With the onset of the primary instability ($\varepsilon = 0$) the liquid layer is tessellated by well-ordered hexagonal cells, $p_7 \sim 0.01$, $p_6 \sim 0.98$, $p_5 \sim 0.01$, $p_4 = 0$. The average number of sides, $\langle n \rangle$, is six and the average vertex coordination number, $\langle \nu \rangle$, is three. The deviation of p_6 from unity is due to a few pentagonal and heptagonal cells, which pair in penta-hepta defects. Beyond ε_p the number of pentagons that are not bound in penta-hepta defects starts to increase, via a mechanism studied in detail in [41]. The process is initiated by a generic transformation of the penta-hepta defect occurring at higher ε, sketched in Fig. 5(a). During this transformation a cell side between the heptagon and one of the hexagons shrinks to vanishing. Consequently, two pentagons and two (nonregular) hexagons appear with a fourfold vertex at the center. Although this *5-5-6-6 cluster* is a topologically stable defect in the larger ε range, it remains only an intermediate step towards larger compounds of pentagons, the *pentalines*. Again, a side of one of the hexagons shrinks to vanishing, and the prototype of the pentaline, comprising four pentagonal cells, appears. The vanishing of cell sides continues and pentalines of growing order, i.e., increasing numbers of pentagons, form [cf. Fig. 5(b), left].

The rise in p_5 accompanies a decrease in $\langle n \rangle$ to 5.5 and an increase in $\langle \nu \rangle$ from three to 3.1. Above $\varepsilon_s = 4.2 \pm 0.3$, square cells appear within the pentalines [Fig. 5(b), right]. A crossover in the topological properties of the pattern sets in. In the range $\varepsilon_s \leqslant \varepsilon \leqslant 5.5$, $\langle n \rangle$ changes from 5.5 to 4.5 while $\langle \nu \rangle$ increases from 3.1 to 3.6. The final state in the experiment, at $\varepsilon = 8.0$ has square convection cells, forming domains of different orientation and extension. The deviation of $\langle \nu \rangle$ and $\langle n \rangle$ from four is due to a few hexagons and pentagons that persist with remarkable stability between the square domains, because of the circular geometry of the container and of the rather high Prandtl number of the liquid [25].

μ_2 measures pattern disorder [12,13], and can describe the transition between two ordered states via a disordered intermediate state. Unlike the defect density [26,27], μ_2 measures deviations from the average value of the entire pattern instead of deviations from the ideal hexagonal lattice, treating hexagonal and square cells equally. The evolution of μ_2 with ε is shown in Fig. 6. In the purely hexagonal regime its value is close to zero. With the rise of the number of pentagons it increases to reach a maximum at $\varepsilon = 4.5$, then decreases to around $\mu_2 \approx 0.4$ at higher ε. The value of $\mu_2 > 0$ at large ε results from the persisting pentagons and hexagons. Comparing the behavior of μ_2 with the shape of p_n, $\langle n \rangle$ and $\langle \nu \rangle$ in Fig. 4, we observe that the μ_2 maximum occurs for the state with maximum p_5 and separates the states dominated either by hexagons or squares. This conformity is not trivial because $\mu_2 = \Sigma_n (n - \langle n \rangle)^2 p_n = p_5[1 + 4(p_4/p_5)] - p_5^2[1 + 4(p_4/p_5) + 4(p_4/p_5)^2]$ (with $p_6 = 1 - p_4 - p_5$ and $\langle n \rangle = \Sigma_n n p_n = 6 - 2p_4 - p_5$). The dependence of μ_2 on the ratio p_4/p_5 and therefore on the size and shape of the different patches requires either extremal p_4/p_5 or $p_6 = p_4$ in order to find simultaneous maxima of μ_2 and p_5 [42]. The state with maximal p_5 is also the state with the maximal number of different patches—the best mixed state.

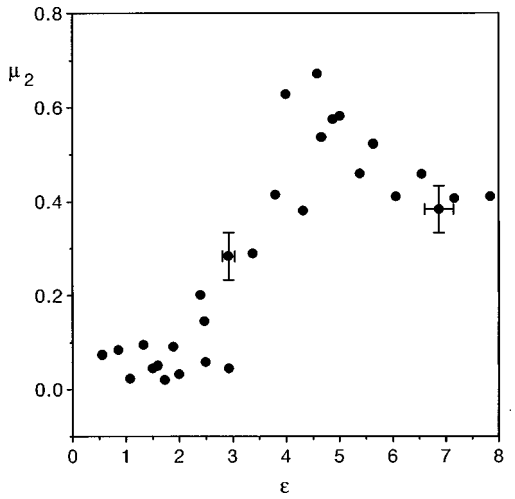

FIG. 6. Second moment of the number of sides distribution, μ_2, as a function of ε. The maximum of μ_2 coincides with the maximum fraction of pentagons.

Furthermore, the appearance of the square cells within the pentalines suggests that the pentagons are not a by-product of the finite geometry but a necessary precondition for the onset of the transition. As discussed in [41] the pentalines introduce a significant curvature in the three elementary roll systems composing the hexagonal pattern. This curvature is a source of the mean flow, also supporting further merging of the cell knots. Thus, the pentagons mediate between the two ordered states. In addition, they introduce significant disorder into the pattern, which is well characterized by μ_2.

B. Metric properties of Bénard cells

1. The metrics of the entire Bénard pattern

Before we look at particular cell classes we first wish to study the entire pattern as a function of ε. According to Table I, we plot in Fig. 7 the average side angle, side length, area, and perimeter. The side angle measures symmetry changes. It is 120 ° in the purely hexagonal regime for $\varepsilon < 1$ and tends to 90° beyond $\varepsilon = 5.5$ where squares dominate (actually ≈ 97 ° because of defects).

The average side length increases slowly with ε both in the hexagon-pentagon regime, $0 \leqslant \varepsilon \leqslant \varepsilon_s$, and in the square-dominated regime above $\varepsilon = 5.5$, due to an increase of wave number [21,20]. Between these ranges, i.e., with the onset of the hexagon-square transition, $\langle l \rangle$ increases by 35%. This increase is much less pronounced in the average perimeter $\langle \pi \rangle$ and not identifiable in $\langle a \rangle$. The behavior of $\langle \pi \rangle$ is a consequence of the contrary behaviors of $\langle l \rangle$ and $\langle n \rangle$ (cf. Fig. 4), which are related to $\langle \pi \rangle$ via Eq. (5). Both $\langle \pi \rangle$ and $\langle a \rangle$ have their slope with ε reduced for $\varepsilon \geqslant 3$ by the growing number of pentagons.

The difference of the dependence of the integral quantities $\langle l \rangle$, $\langle \pi \rangle$, and $\langle a \rangle$ on ε suggests that the ratio between perimeter $\langle \pi \rangle$ and area $\langle a \rangle$ affects pattern evolution. In Fig. 8 we plot $\langle \pi \rangle$ versus $\langle a \rangle$ with ε as a parameter. Since both $\langle \pi \rangle$ and $\langle a \rangle$ grow monotonically with ε, points located near the origin have lower ε. With the onset of the hexagon-square transition at $\varepsilon = \varepsilon_s$ the points deviate more and more from the dotted line. Thus, in this regime, $\langle \pi \rangle$ increases more rapidly than for $\varepsilon < \varepsilon_s$. To understand this behavior we study next the behaviors of particular cell classes.

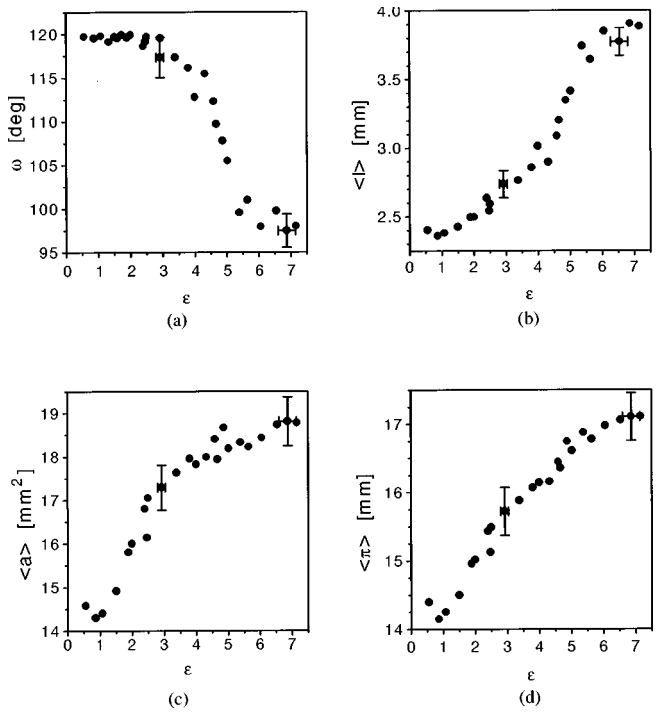

FIG. 7. The metric properties of Bénard cells as a function of ε. (a) Average side angle $\langle \omega \rangle$, (b) average side length $\langle l \rangle$, (c) average cell area $\langle a \rangle$, and (d) average cell perimeter $\langle \pi \rangle$.

2. The properties of hexagonal, square, and pentagonal Bénard cells

Unlike Fourier space analysis, SGPN allows us to obtain a complete set of averaged metric quantities for all three cell types, including cell area and perimeter. Furthermore, SGPN can provide all minimal spanning tree results, with the

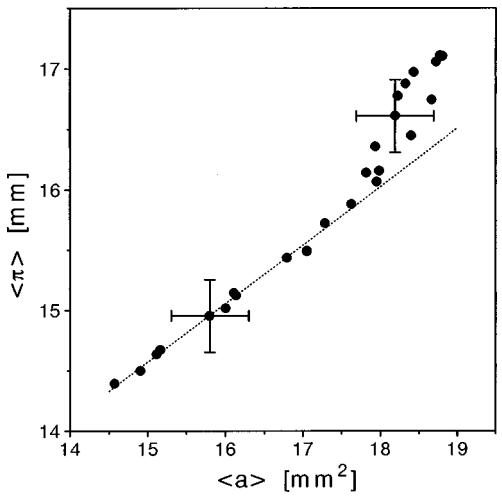

FIG. 8. Average cell perimeter $\langle \pi \rangle$ vs average cell area, $\langle a \rangle$. ε increases monotonically from left to right. The dotted line is a guide line. All points deviating clearly from this line have $\varepsilon \geqslant \varepsilon_s$.

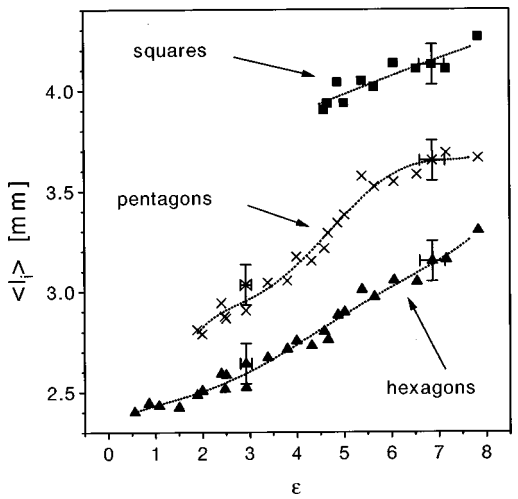

FIG. 9. Dependence of the average side length on ε for the three cell classes. The dotted lines are guide lines.

branch length distribution and its second moment replaced by the normalized side length distribution and its second moment.

Figure 9 plots the average side length for each cell class. Comparing the values of $\langle l_n \rangle$ we find that the square (hexagonal) cells have the highest (lowest) side lengths while pentagons are intermediate. In the transition range, $\varepsilon_s \leqslant \varepsilon \leqslant 5.5$, the pentagon side length $\langle l_5 \rangle$ displays a peculiar behavior. While $\langle l_6 \rangle$ changes in this range by about 5%, $\langle l_5 \rangle$ increases by 10%. Thus, the pentagons behave like hexagons (squares) if most cells are hexagonal (square). Knowing the behavior of $\langle l_n \rangle$ allows us to understand the evolution of the integral quantity $\langle l \rangle$ [cf. Fig. 7(b)]. The drastic change starting at $\varepsilon = \varepsilon_s$ is caused by the crossover from the hexagon line, $\langle l_6 \rangle$, to the square line, $\langle l_4 \rangle$, due to the stability loss of the hexagons. It is further supported by the behavior of the pentagons mediating between both cell classes. In Table IV we compare the fits $\langle a_n \rangle$ versus $\langle l_n \rangle$ with the relations expected for strictly regular cells. The deviation of the prefactors from regularity is 0.4% for squares, 2.7 % for pentagons, and 1.9% for hexagons. The irregularity changes the relations between side length and wave number for regular polygons:

$$k_6 = \frac{4\pi}{3 l_6}, \quad k_4 = \frac{2\pi}{l_4}. \tag{11}$$

Therefore, the translation of the wave number measured in Fourier space into side length of the cells via Eq. (11) is only approximate.

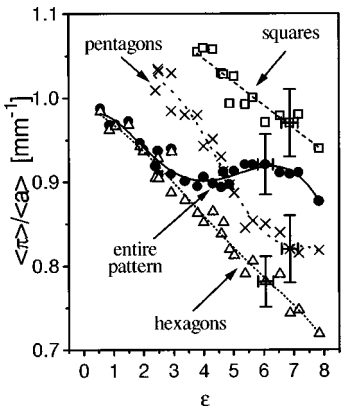

FIG. 10. The ratio $\langle \pi \rangle / \langle a \rangle$ between average perimeter and average area vs the control parameter, ε, for the entire pattern and the three cell types.

Another consequence of the qualitatively different behavior of the $\langle l_n \rangle$ (and therefore of the $\langle \pi_n \rangle$) is that $\langle \pi_n \rangle$ cannot depend linearly on the side number n (Feltham's law). The same argument applies for the linear dependency of the average cell area $\langle a_n \rangle$ on n (Lewis' law). However, the laws might hold in a subrange of the control parameter. Reference [16] validated Lewis' law for $\varepsilon = 2.5$. Our analysis shows that in the weakly nonlinear range both Lewis' and Feltham's law apply reasonably well. As for soap froth [14], the statistical error is slightly less for Feltham's than for Lewis' law.

3. The perimeter-area-ratio criterion

Next we study the $\langle \pi \rangle / \langle a \rangle$ ratios both of the entire pattern and of the particular cell classes (Fig. 10). We see that these quantities decrease with increasing ε, which is due to a global increase of the cell sizes [25]. The $\langle \pi \rangle / \langle a \rangle$ ratio of the entire Bénard pattern moves through the space bounded by the hexagon and the square lines. For $\varepsilon < 2.5$ where hexagons are dominant, the ratio follows the hexagon line. In the transition range, extending from $3.0 \leqslant \varepsilon \leqslant 6.0$ the ratio increasingly deviates from the hexagon line, intersecting the line of pentagons. Above $\varepsilon = 6.0$ the $\langle \pi \rangle / \langle a \rangle$ ratio follows the square line. Figure 10 suggests that the stability loss of hexagons results to a part from an unfavorable perimeter-area ratio in comparison to square cells. Indeed, we find that $\langle \pi_4 \rangle / \langle a_4 \rangle$ drastically exceeds the values expected on the basis of the following two arguments. Generally, the relation

$$\frac{\langle \pi_4 \rangle / \langle a_4 \rangle}{\langle \pi_6 \rangle / \langle a_6 \rangle} = \sqrt{3}\ \frac{\langle l_6 \rangle}{\langle l_4 \rangle} \tag{12}$$

TABLE IV. The relation between average side length, $\langle l_n \rangle$, and average cell area, $\langle a_n \rangle$, for the three cell classes.

Planform	Theoretical relation for the regular planform	Relation as determined from experiment
Hexagonal cell	$a_6 = \frac{3}{2}\sqrt{3} l_6^2 = 2.598 l_6^2$	$\langle a_6 \rangle = 2.550 \langle l_6 \rangle^2$
Pentagonal cell	$a_5 = \frac{1}{4}\sqrt{25 + 10\sqrt{5}}\, l_5^2 = 1.720 l_5^2$	$\langle a_5 \rangle = 1.673 \langle l_5 \rangle^2$
Square cell	$a_4 = l_4^2$	$\langle a_4 \rangle = 0.996 \langle l_4 \rangle^2$

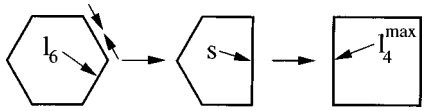

FIG. 11. Schematic of the derivation of an upper bound for the side length of a square cell, l_4, as a function of the side length l_6 of the hexagonal cell.

holds for regular planforms (cf. Table IV), i.e., the ratio of the $\langle \pi_n \rangle / \langle a_n \rangle$ is inversely proportional to the ratio of the side lengths. A $\langle \pi_4 \rangle / \langle a_4 \rangle$ larger than $\langle \pi_6 \rangle / \langle a_6 \rangle$ requires

$$\langle l_4 \rangle \leqslant \sqrt{3}\ \langle l_6 \rangle. \tag{13}$$

To estimate $\langle l_4 \rangle$ we consider first the real transition as sketched schematically in Fig. 11. The largest side length, s, of the pentagon gives an upper bound for $\langle l_4 \rangle$ as, $s = l_4^{\max} = 2 l_6 \sin \pi/3 = \sqrt{3}\ l_6$. From this argument we obtain $\langle \pi_4 \rangle / \langle a_4 \rangle = \langle \pi_6 \rangle / \langle a_6 \rangle$. We next consider an ideal transition that proceeds directly from hexagons to squares. The conservation of the cell area requires $l_4 = \sqrt{\sqrt{3}/2}\sqrt{3}\ l_6$, implying $(\langle \pi_4 \rangle / \langle a_4 \rangle) / (\langle \pi_6 \rangle / \langle a_6 \rangle) = \sqrt{2/\sqrt{3}} \approx 1.07$. In the experiment, however, we find $\langle l_4 \rangle = (0.80 \pm 0.03)\sqrt{3}\ \langle l_6 \rangle$ leading to

$$\frac{\langle \pi_4 \rangle / \langle a_4 \rangle}{\langle \pi_6 \rangle / \langle a_6 \rangle} = (1.26 \pm 0.05). \tag{14}$$

The difference between the observed (1.26) and the maximum expected (1.07) values is also qualitative. Assuming Eq. (11) for regular polygons, i.e., $k_4 / k_6 = 3 l_6 / 2 l_4$, the two considerations above imply a wave number ratio between

$$0.87 < \frac{k_4}{k_6} < 0.93. \tag{15}$$

The upper (lower) value is valid for argument one (two). The wave number of squares should be at least 7% smaller than that of hexagonal cells. The wave number ratio observed in the experiment, however, is *larger* than unity by nearly 7%, in accordance with results obtained independently by Fourier space analysis [25].

To see why the higher perimeter-area ratio favors square cells at larger ε we briefly recall the main feature of strongly nonlinear STDBC [43]. For increasing ε the Peclet number Pe rises while the Reynolds number remains below unity. Due to the high Peclet number the isotherms are strongly deformed even at moderate ε. The nonlinear redistribution of the temperature gradients leads to the formation of thermal boundary layers of thickness δ between adjacent cells. This scale separation into a macro scale, k^{-1}, and a micro scale, $\delta \sim (k\mathrm{Pe})^{-1}$, expresses the asymmetry between up and down flow and is independent of the cell shape. For increasing ε the rising hot liquid occupies more and more of the cell, while the area available for the down flow shrinks to $a_- \sim \pi\delta$, where π equals the cell perimeter.

For any plane parallel to the bottom of a cell with cross section a,

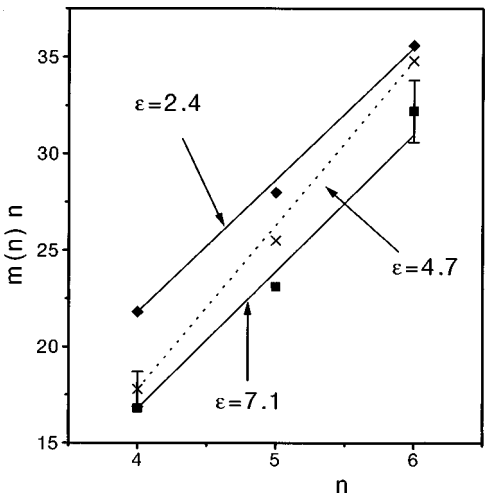

FIG. 12. The dependence of $m(n)n$ on n (Aboav-Weaire law). The lines represent the linear relation Eq. (6) with a_W calculated by a least squares fit. We show one mainly hexagonal network ($\varepsilon = 2.4$), a network from the transition region ($\varepsilon = 4.7$) and a network with mainly square cells ($\varepsilon = 7.1$).

$$\int \int_a v_z(x,y,z=\mathrm{const})\ dx\ dy = 0,$$

requiring $v_z^+ a_+ \approx v_z^- a_-$ with $a = a_- + a_+$ where "+" refers to up flow. Since $a_- \ll a_+$ it follows that $a_+ \approx a$. Given an average upward velocity, v_z^+, the downward velocity is higher for smaller areas of down flow and becomes roughly proportional to $(\pi/a)^{-1}$. Thus, the square cells convert the thermocapillary energy more efficiently at higher ε, since the viscous dissipation associated with the vertical motion is obviously smaller.

C. The relation between topological quantities

Until now we have analyzed the metric and topological quantities of single cells averaged over the ensemble. Next we focus on correlations between the topological properties of neighboring cells. Especially, we check the generalized Aboav-Weaire-law [Eq. (6)], calculating the Aboav parameter a_W from the experimental data via the weighted linear fit $m(n)n = c_l n + c_c$. Comparing with Eq. (6) we obtain $a_W = \langle n \rangle - c_l$. The validity of the law in our case requires $c_c = \langle n \rangle a_W + \mu_2$, and the mean deviation is less then 2%. Thus, our data support the applicability of the Aboav-Weaire law to patterns with threefold *and* fourfold vertices. This fact is surprising, since the Bénard pattern differs significantly from the usually studied random networks, with cells preferentially clustering with cells of the same topological class. This circumstance distinguishes the Bénard pattern from stochastical networks like soap froth.

In Fig. 12 we show the dependence of $m(n)n$ on n for three different ε, the beginning, middle, and end of the hexagon-square transition. With increasing ε, the curves shift towards smaller values of $m(n)n$, while the slope changes nonmonotonically. In the range $2.7 \leqslant \varepsilon \leqslant 4.8$ the slope increases from 6.5 to 8.5, then decreases almost to its starting value at about $\varepsilon = 6.6$. The slope is generally larger than the value of 5 typical for random networks like soap

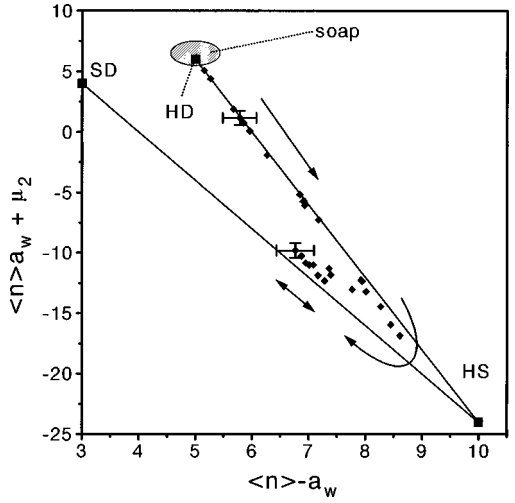

FIG. 13. The constant coefficient of the Aboav-Weaire law, $\langle n\rangle a_W+\mu_2$, vs the linear coefficient, $\langle n\rangle-a_W$. The upper straight line connects HS with a regular hexagonal network with one 5-7 defect (HD). The lower straight line connects HS with a regular square network with one 3-5 defect (SD). The arrows indicate increasing ε.

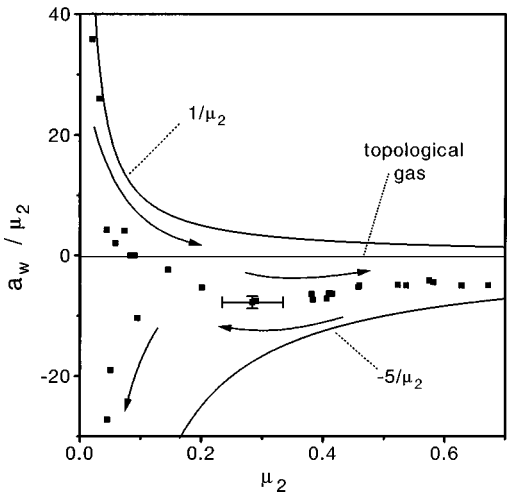

FIG. 14. The quotient a_W/μ_2 vs μ_2. The curve $1/\mu_2$ results from the theoretical value $a_W=1$. The lower limit in a_W/μ_2 for networks with only threefold vertices is set by the topological gas with $a_W/\mu_2=-1/6$. It separates the realms of negative and positive correlation. The lower boundary is given by an extended HS pattern that gives the curve $-5/\mu_2$. Arrows indicate increasing ε.

froth or epidermal tissue [15]. The maximum for the Bénard pattern is $\langle n\rangle-a_W\approx 8.5$, close to the value $\langle n\rangle-a_W=10$ that we show below to be a general upper bound for networks that contain exclusively squares, pentagons, and heptagons.

A prototype of such a pattern (denoted by HS) consists of many large homogeneous patches of hexagonal and square cells, separated by lines of pentagons. Assuming this pattern is infinite and the number of cells in the patches is very large in comparison to the number of pentagons, we have $m(4)n=16$, $m(5)n=26$ [44], $m(6)n=36$. The dependence of $m(n)n$ on n is linear with a slope of $\langle n\rangle-a_W=10$. Since $\langle n\rangle=5$, $a_W=-5$. Because $\mu_2=1$, the constant coefficient in the Aboav-Weaire law has a value of $\langle n\rangle a_W+\mu_2=-24$, the constant coefficient c_c of the linear fit for HS. Looking at the HS pattern we can understand the increase of the slope in the transition region. In the nearly ordered hexagonal (square) pattern below (above) the transition, square (hexagonal) cells act as defects in the transition region. The two different ordered states coexist in a manner resembling the limiting case of HS.

The patterns below and above the transition are clearly distinguished by their topological correlations. Figure 13 shows the calculated constant coefficient $\langle n\rangle a_W+\mu_2$ of Eq. (6) as a function of the slope $\langle n\rangle-a_W$. The data points are bounded by two straight lines representing ideal transitions from the hexagonal (square) pattern to the mediating HS pattern and therefore characterizing two different regimes for the neighboring cell correlations of the Bénard pattern. The upper line connects the HS pattern to a hexagonal pattern with a small number of 5–7 defects (HD). The HD pattern has a slope $\langle n\rangle-a_W=5$ and a constant coefficient $\langle n\rangle a_W+\mu_2=c_c=6$. The lower line connects the HS pattern to a square pattern with a small number of 3–5 defects called SD. The slope is $\langle n\rangle-a_W=3$ and the constant coefficient $\langle n\rangle a_W+\mu_2=c_c=4$. Small numbers of defects mean that defects are completely embedded in the ordered hexagonal (square) pattern and therefore do not neighbor each other. The data points belonging to small ε start at the upper line. With increasing ε they move down along the upper line, diverging slowly. At about $\varepsilon=4.8$ the pattern jumps to the lower line and then travels erratically along this line as indicated by the arrows. Random networks like two-dimensional soap froth have typical slopes of $\langle n\rangle-a_W\approx 5$. In Fig. 13 they lie just above the upper solid line.

Figure 14 plots the quotient a_W/μ_2 as a function of μ_2, allowing us to distinguish the Bénard pattern from a wide range of naturally occurring patterns [45]. The data points are confined by two lines. The curve $a_W/\mu_2=1/\mu_2$ results from the theoretical value $a_W=1$ [15] and gives an approximate upper bound. The networks compared in [45] lie in its vicinity. A lower boundary is given by the extended HS pattern, in which the ratio of pentagons to squares and hexagons varies, resulting in $a_W=-5$ but different μ_2. Consequently, the lower limiting curve is given by $a_W/\mu_2=-5/\mu_2$.

A network without any neighboring cell correlations, a topological gas, sets another lower limit of a_W/μ_2 for networks with threefold vertices only with $a_W/\mu_2=-1/6$ [46]. In the absence of fourfold vertices the Bénard patterns stay above this gas line. Their topological correlations are comparable to weakly disordered soap froth [16]. As soon as fourfold vertices appear, the patterns move below this limiting value. We call the regimes above and below the gas line, $a_W/\mu_2=-1/6$, negative and positive correlation, respectively.

Positive correlation implies that cells of different topological class exist but all cells tend to cluster with cells of the same topological class, as for the hexagonal and square cell domains of STDBC. Positive correlation can only occur if vertices with different coordination numbers are allowed. Negative correlation describes cells clustered with cells of different topological class, which is typical for disordered soap froth or grain boundaries. Ordered networks consisting of cells of one topological class only do not fall into this classification.

D. Finite size effects

Are our statistics strongly influenced by finite size effects? Even stochastic networks with vertices of coordination 3 have average numbers of sides $\langle n\rangle \leqslant 6$ for few cells. The influence of finite size depends on the number of cells, on the number of cells at the boundary of the pattern, and on the number of vertices at the boundary where fewer than three sides meet.

Existing formulas [47] work for $\langle \nu\rangle = 3$ only. However, two alternative ways are based on Eqs. (3) and (5), which are strictly valid for *infinite* networks. Since both equations yield an error of the same order, we restrict ourselves to Eq. (3), which allows us to calculate a theoretical average number of sides $\langle n\rangle_\infty$ from $\langle \nu\rangle$. The average coordination $\langle \nu\rangle$ is not influenced by the finite size of our sample because the incomplete cells at the rim are excluded. The difference, Δn, between $\langle n\rangle_\infty$ and the measured $\langle n\rangle$ gives a quantitative estimate of finite size effects. The relative error $|\Delta n/\langle n\rangle_\infty|$ is always below 2%. Thus, the influence of finite size effects on the results is weak.

IV. SUMMARY AND CONCLUSIONS

We have analyzed the topological and metric properties of Bénard-Marangoni cells in the framework of stochastic geometry. This statistical approach based on the tabulation of the coordinates of the vertices of all cells, as well as of all the neighborship relations, provides the distributions of all topological and metric variables of the cell network.

The topology of the Bénard pattern is described by the number of sides and the vertex coordination number distributions. At the onset of the hexagon-square transition, both quantities undergo drastic opposing changes. The average side number falls from six towards four and the vertex coordination number rises from three towards four. The second moment of the side number distribution characterizes the degree of topological disorder in the pattern, its maximum correlating with the maximum number of pentagons.

The dependency on ε of the integral metric quantities, average side length, cell perimeter, and cell area of the entire pattern is qualitatively different, and cannot be deduced from any of these variables. With onset of the hexagon-square transition, the average perimeter increases faster than the cell area suggesting that the ratio between both quantities affects the planform change of STDBC. Indeed, the perimeter-area ratio of a square Bénard cell exceeds that of a hexagonal one by approximately 25%, nearly 20% higher than predicted.

The SGPN allows us to quantify the properties of pentagonal cells in detail. The side length, perimeter, and cell area of pentagons lie between hexagons and squares. In the transition range from hexagons to squares, $\varepsilon_s \leqslant \varepsilon \leqslant 5.5$, the metric quantities of the pentagons change more rapidly than those of the other cell types. This behavior expresses the chameleon-like character of the pentagons, which behave like hexagons if hexagons dominate and like squares if squares dominate.

The Bénard-Marangoni cells obey the generalized Aboav-Weaire law, extending the range of validity of the law from random networks with threefold vertices to networks including fourfold vertices. We have proved the strict validity of the law for a model network that resembles the Bénard pattern in the transition region. Topological correlation distinguishes among polygonal patterns. For positive topological correlation the cells cluster with cells of the same topological class. While random patterns like disordered soap froth are negatively correlated, the polygonal cells in STDBC are positively correlated as soon as fourfold vertices appear.

In comparison to other methods, the statistics of polygonal networks offer some advantages. The technique produces simple statistics in physical space, and can easily handle symmetry changes within a polygonal structure since it makes no use of a specific reference. It calculates both the topological quantities of the entire pattern and the metric properties of each cell.

Our analysis suggests that the metric properties of a cell influence its stability at a given value of the control parameter. A numerical check of this assumption would be useful. The method proposed is not restricted to STDBC. It should apply to other polygonal systems in hydrodynamics like Rayleigh-Bénard convection with strongly temperature-dependent viscosity [48] or solutal Marangoni convection [49].

ACKNOWLEDGMENTS

We are grateful to H. Wendrock for sharing his image processing routine, to D. Weise for help with programming, and to H. Kantz, N. Rivier, G. Schliecker, and A. Thess for interesting discussions.

[1] F. T. Lewis, Anat. Rec. **38**, 341 (1928).
[2] F. T. Lewis, Anat. Rec. **50**, 235 (1931).
[3] F. T. Lewis, Am. J. Bot. **30**, 766 (1943).
[4] F. T. Lewis, Am. J. Bot. **31**, 619 (1944).
[5] J. C. M. Mombach, M. A. Z. Vasconcellos, and R. M. C. de Almeida, J. Phys. D **23**, 600 (1990).
[6] J. C. M. Mombach, R. M. C. de Almeida, and J. R. Iglesias, Phys. Rev. E **47**, 3712 (1993).
[7] C. S. Smith, *Metal Interfaces* (American Society for Metals, Cleveland, OH, 1952), p. 65.
[8] D. A. Aboav, Metallography **13**, 43 (1980).
[9] D. A. Aboav, Metallography **16**, 265 (1983).
[10] D. A. Aboav, Metallography **17**, 383 (1984).
[11] D. A. Aboav, Metallography **18**, 129 (1985).
[12] J. A. Glazier, S. P. Gross, and J. Stavans, Phys. Rev. A **36**, 306 (1987).
[13] J. A. Glazier, S. P. Gross, and J. Stavans, Nucl. Phys. B **2**, 570 (1987).
[14] K. Y. Szeto and W. Y. Tam, Physica A **221**, 256 (1995).
[15] D. Weaire and N. Rivier, Contemp. Phys. **25**, 59 (1984).
[16] P. Cerisier, S. Rahal, and N. Rivier, Phys. Rev. E **54**, 5086 (1996).
[17] H. Bénard, Rev. Gén. Sci. Pures Appl. **11**, 1261 (1900).
[18] E. L. Koschmieder and M. I. Biggerstaff, J. Fluid Mech. **167**, 49 (1986).
[19] M. F. Schatz, S. J. Van-Hook, W. D. Mc Cormick, J. B. Swift,

and H. Swinney, Phys. Rev. Lett. **75**, 1938 (1995).
[20] E. L. Koschmieder and D. W. Switzer, J. Fluid Mech. **240**, 533 (1992).
[21] P. Cerisier, C. Perez-Garcia, C. Jamond, and J. Pantaloni, Phys. Rev. A **35**, 1949 (1987).
[22] P. Cerisier, C. Perez-Garcia, and R. Occelli, Phys. Rev. E **47** , 3316 (1993).
[23] K. Nitschke-Eckert and A. Thess, Phys. Rev. E **52**, R5772 (1995).
[24] M. Bestehorn, Phys. Rev. Lett. **76**, 46 (1996).
[25] K. Eckert, M. Bestehorn, and A. Thess, J. Fluid Mech. **356** , 155 (1998).
[26] R. Occelli, E. Guazzelli, and J. Pantaloni, J. Phys. (France) Lett. **44**, L567 (1983).
[27] P. Cerisier, R. Occelli, C. Perez-Garcia, and C. Jamond, J. Phys. (France) **48**, 569 (1987).
[28] P. Cerisier, H. Nguyen Thi, and B. Billia, Physica D **61**, 113 (1992).
[29] N. Rivier, R. Occelli, J. Pantaloni, and A. Lissowski, J. Phys. (France) **45**, 49 (1984).
[30] N. Rivier, J. Phys. (France) **4**, 931 (1992).
[31] D. Stoyan, W. S. Kendall, and J. Mecke, *Stochastic Geometry and its Applications* (Akademie Verlag/J. Wiley, Berlin/ Chichester, 1987).
[32] H. Hermann, *Stochastic Models of Heterogeneous Materials* (Trans Tech Publications Ltd., Zürich, 1991).
[33] R. V. Ambatzumjan, J. Mecke, and D. Stoyan, *Geometrische Wahrscheinlichkeiten und Stochastische Geometrie* (Akademie Verlag, Berlin, 1993).
[34] G. le Caër and R. Delannay, J. Phys. A **26**, 3931 (1993).
[35] G. le Caër and R. Delannay, J. Phys. I (France) **3**, 1777 (1993).
[36] V. Pignol, R. Delannay, and G. le Caër, Acta Stereol. **12**, 149 (1993).
[37] S. N. Chiu, Mater. Charact. **34**, 149 (1995).
[38] E. L. Koschmieder and S. G. Pallas, Rev. Sci. Instrum. **45**, 1164 (1974).
[39] W. Merzkirch, *Flow Visualization* (Academic Press, New York, 1974).
[40] J. Pantaloni and P. Cerisier, in *Cellular Structures in Instabilities*, edited by J. E. Wesfreid and S. Zaleski (Springer, Berlin, 1984).
[41] K. Eckert and A. Thess (unpublished).
[42] The derivative $\partial\mu_2/\partial\varepsilon = 4\,p_5\,\partial(p_4/p_5)/\partial\varepsilon\,(p_6-p_4)$ is zero if the number of hexagons equals the number of squares or (p_4/p_5) has an extremal value.
[43] A. Thess and S. A. Orszag, J. Fluid Mech. **283**, 201 (1995).
[44] The pentagons in the lines separating square and hexagon patches have one square, two pentagons and two hexagons as neighbors. Thus, $m(5)=(1\times4+2\times5+2\times6)/5$.
[45] R. Delannay and G. le Caër, Phys. Rev. Lett. **73**, 1553 (1994).
[46] V. E. Fradkov, L. S. Shindlerman, and D. G. Udler, Philos. Mag. Lett. **55**, 289 (1987).
[47] M. A. Fortes and A. C. Ferro, Acta Metall. **33**, 1697 (1985).
[48] D. B. White, J. Fluid Mech. **191**, 247 (1988).
[49] H. Linde, in *Convective Transport and Instability Phenomena*, edited by J. Zierep and H. Oertel, Jr. (G. Braun, Karlsruhe, 1982), and references therein.